Electromagnetic excitation of particle suspensions in hydraulic fractures using a coupled lattice Boltzmann-discrete element model

Citation: Leonardi, Christopher R. et al. "Electromagnetic Excitation of Particle Suspensions in Hydraulic Fractures Using a Coupled Lattice Boltzmann-Discrete Element Model." Computational Particle Mechanics 3.2 (2016): 125–140.

As Published: http://dx.doi.org/10.1007/s40571-015-0035-x

Publisher: Springer International Publishing

Persistent URL: http://hdl.handle.net/1721.1/103302

Version: Author's final manuscript: final author's manuscript post peer review, without publisher's formatting or copy editing

Computational Particle Mechanics manuscript No.
(will be inserted by the editor)

Electromagnetic excitation of particle suspensions in hydraulic fractures using a coupled lattice Boltzmann-discrete element model

Christopher R. Leonardi · Jon W. S. McCullough · Bruce D. Jones · John R. Williams

Received: date / Accepted: date

Abstract This paper describes the development of a computational framework that can be used to describe the electromagnetic excitation of rigid, spherical particles in suspension. In this model the mechanical interaction and kinematic behaviour of the particles is modelled using the discrete element method, while the surrounding fluid mechanics is modelled using the lattice Boltzmann method. Electromagnetic effects are applied to the particles as an additional set of discrete element forces, and the implementation of these effects was validated by comparison to the theoretical equations of point charges for Coulomb's law and the Lorentz force equation. Oscillating single and multiple particle tests are used to investigate the sensitivity of particle excitation to variations in particle charge, field strength, and frequency. The further capabilities of the model are then demonstrated in a numerical illustration, in which a hydraulic fracture fluid is excited and monitored within a hydraulic fracture. This modelling explores the feasibility of using particle vibrations within the fracture fluid to aid in the monitoring of fracture propagation in unconventional gas reservoirs.

This work was supported in part by the MITei-Saudi Aramco Seed Fund Scheme and this is gratefully acknowledged by the authors.

C. R. Leonardi and J. W. S. McCullough
The University of Queensland, School of Mechanical and Mining Engineering, Cooper Rd, St Lucia QLD 4072, Australia
E-mail: c.leonardi@uq.edu.au, j.mccullough@uq.edu.au

C. R. Leonardi, B. D. Jones and J. R. Williams
Massachusetts Institute of Technology, Department of Civil and Environmental Engineering, 77 Massachusetts Avenue, Cambridge MA 02139, USA
E-mail: chrisleo@mit.edu, bdjones@mit.edu, jrw@mit.edu

Keywords non-colloidal suspensions · electromagnetic excitation · lattice Boltzmann method · discrete element method · hydraulic fracturing

1 Introduction

Particle suspensions, typically comprised of a collection of discrete solids dispersed throughout an encompassing fluid medium, are of importance in a broad range of scientific and engineering disciplines. Applications include concrete in construction, hydraulic fracturing and drilling fluids in the oil and gas industry, management of mining waste, industrial manufacture processes and the study of biological fluids. The customisation of such mixtures towards a specific purpose can be achieved by modifying the properties of the constituent phases, such as the shape or size distribution of the solid phase or the viscosity of the fluid phase.

The characterisation of particle suspensions, as well as the design of new and novel formulations, has traditionally been informed by experiments. However, emerging techniques in computational modelling present an opportunity for suspension designs to be tested prior to prototyping. Continued development and improvement in the modelling of suspensions with novel fluid-solid properties would allow more accurate characterisation and optimisation, thereby increasing the scope of their practical applications.

This paper presents the development of a numerical model which applies an oscillating electromagnetic field to a suspension of charged particles. This has been achieved through the coupling of the discrete element method (DEM), which is used to model the particle phase, to the lattice Boltzmann method (LBM), which is used to model the fluid behaviour. The electromag-

netic forces that act on the particles have been explicitly applied via the DEM component of the framework. This model has been used to develop a qualitative and quantitative understanding of the effect that parameters such as field oscillation frequency, field amplitude and particle charge have on the behaviour of the suspension.

This work has been separated into four further sections. Section 2 provides a brief description of the DEM and LBM as employed in this work, along with the necessary background theory of electromagnetics that have been implemented by the model. In Section 3 the model is verified and validated by comparison to theoretical relations and then used to understand the sensitivity of particle excitation to changes in the electromagnetic field and particle charge. The capabilities of the developed model are illustrated in Section 4 via an investigation of the excitation of a hydraulic fracturing fluid in a candidate fracture geometry. A discussion of the implementation and application of the model is presented in Section 5 along with some concluding remarks.

2 LBM-DEM Modelling with Electromagnetic Behaviour

The suspension modelling undertaken in this study uses the DEM and the LBM to describe the kinematics of individual particles and the hydrodynamics of the suspending fluid, respectively. Since it was first proposed, the coupling of the LBM to particles [1,2], and then more formally to the DEM [3,4], has proved popular due to its ability to model the interaction of fluids and solids in the presence of evolving boundaries and multiple particle contacts. A significant advantage of the LBM-DEM framework over approaches which use the finite element method (FEM) or smooth particle hydrodynamics (SPH) for the fluid is that the number of spatial discretisation points between DEM particles can readily tend to zero. This and other aspects of the LBM-DEM framework employed in this study are discussed as follows.

2.1 The lattice Boltzmann method

Since its emergence more than a quarter of a century ago, the lattice Boltzmann method has gained traction as a powerful alternative to conventional computational fluid dynamics (CFD). It is now applied in both research and commercial settings to solve a wide array of fluid mechanics problems such as those involving porous media, vehicle aerodynamics, non-Newtonian fluids and particle suspensions.

The LBM [5,6] takes a mesoscopic approach to modelling the mechanics of fluids. In the context of length scales it sits above microscale approaches such as molecular dynamics (MD) and lattice gas automata (LGA) but below macroscale finite difference (FD) and finite volume (FV) approaches which are based on the discretisation of the Navier-Stokes equations. The LBM can itself be interpreted as a particle method with the primary variables viewed as discrete packages of fluid mass and momentum. The temporal evolution of these packages is updated using an explicit time integration scheme but, unlike in MD or SPH, the evolution is constrained to a discrete velocity space.

The primary variables of the LBM are the particle distribution functions, f_i, which reside at each node throughout the domain. Each distribution function can be interpreted as the probability of finding a molecule of fluid moving with a certain momentum at a certain point in space and time. The kernel processes of the LBM are the streaming and collision functions. The former advects the particle distribution functions to their target neighbour node whilst the latter relaxes the functions colliding at a node towards an equilibrium value. This stream-collide sequence is performed at each time step and described by the lattice Boltzmann equation,

$$f_i(\mathbf{x}+\mathbf{c}_i\Delta t, t+\Delta t) = f_i(\mathbf{x},t) - \frac{\Delta t}{\tau}(f_i(\mathbf{x},t) - f_i^{eq}(\mathbf{x},t)), \tag{1}$$

in which $f_i(\mathbf{x},t)$ is the particle distribution function with velocity $\mathbf{c}_i$ $[m/s]$ at a node located at position $\mathbf{x}$ for a given time t, and Δt is the time step $[s]$. Here, the single-relaxation-time Bhatnagar-Gross-Kross (BGK) collision operator [7–9] is used, in which τ $[s]$ is the relaxation time and f_i^{eq} is the equilibrium distribution function based on a truncated form of the Maxwellian distribution.

The number of particle distribution functions associated with each LBM node is dependent on the lattice that is used to discretise the fluid domain. Here the $D3Q15$ lattice, as shown in Figure 1, is used as it has been shown [10] to represent a good compromise between computational efficiency and simulation accuracy. This lattice is comprised of one rest function ($i = 0$), six orthogonal neighbour functions ($i = 1-6$, distance of 1), and eight bi-diagonal neighbour functions ($i = 7-14$, distance of $\sqrt{3}$). Other lattice options in the three-dimensional LBM include $D3Q18$, $D3Q19$, and $D3Q27$. Maier et al. [11] showed that, although accuracy does increase with the number of lattice directions, it does not necessarily justify the increase in computational overhead.

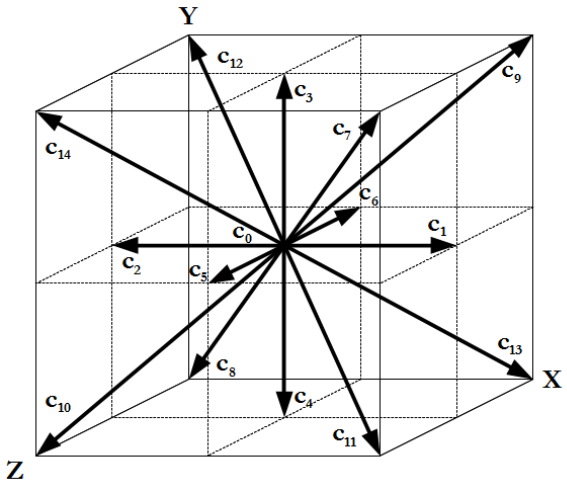

Fig. 1 Spatial discretisation using the $D3Q15$ lattice, showing the rest function, c_0, and the 14 lattice neighbours, c_{1-14}.

The calculation of macroscopic fluid variables in the LBM is straightforward. Both nodal density,

$$\rho = \sum_i f_i, \tag{2}$$

and momentum flux,

$$\rho \mathbf{u} = \sum_i f_i \mathbf{c}_i, \tag{3}$$

are defined as local moments of the particle distribution functions, with $\mathbf{u}$ the macroscopic fluid velocity $[m/s]$.

The LBM equilibrium functions can be viewed as small-velocity expansions of the Maxwell-Boltzmann distribution [1] with adjustable coefficients. For the $D3Q15$ lattice used in this study the equilibrium functions can be written for $i = 0$ as,

$$f_i^{eq} = \frac{2\rho}{9}\left[1 - \frac{3}{2c^2}(\mathbf{u}\cdot\mathbf{u})\right], \tag{4}$$

and for $i = 1-6$ as,

$$f_i^{eq} = \frac{\rho}{9}\left[1 + \frac{3}{c^2}(\mathbf{c}_i\cdot\mathbf{u}) + \frac{9}{2c^4}(\mathbf{c}_i\cdot\mathbf{u})^2 - \frac{3}{2c^2}(\mathbf{u}\cdot\mathbf{u})\right], \tag{5}$$

and for $i = 7-14$ as,

$$f_i^{eq} = \frac{\rho}{72}\left[1 + \frac{3}{c^2}(\mathbf{c}_i\cdot\mathbf{u}) + \frac{9}{2c^4}(\mathbf{c}_i\cdot\mathbf{u})^2 - \frac{3}{2c^2}(\mathbf{u}\cdot\mathbf{u})\right], \tag{6}$$

in which $c = \Delta x/\Delta t$ is the lattice speed $[m/s]$ and Δx is the grid spacing $[m]$.

Using a multiscale Chapman-Enskog analysis it can be shown that, at the macroscale, the LBM recovers the Navier-Stokes equations in the near-incompressible limit [12]. This procedure takes as input the lattice Boltzmann equation, the lattice geometry, and the general form of the equilibrium functions and, as by-products, defines the coefficients of the equilibrium functions along with an equation of state for pressure $[Pa]$,

$$p = \frac{c^2\rho}{3}, \tag{7}$$

and the relationship between the BGK relaxation parameter, τ, and the kinematic viscosity of the fluid $[m^2/s]$,

$$\nu = \frac{1}{3}\left(\tau - \frac{1}{2}\right)\frac{(\Delta x)^2}{\Delta t}. \tag{8}$$

The numerical (not physical) compressibility of the LBM is evident from the definition of pressure in Equation 7. From Equation 8, and the requirement of positive viscosity, the need for $\tau > 1/2$ is also apparent. Further details on the stability of the LBM can be found in the work of Sterling and Chen [13]. The small-velocity expansion used in the Chapman-Enskog analysis also places an upper limit on the Mach number, $Ma = u/c_s$, of the computations, where $Mc_s = c/\sqrt{3}$ is the lattice speed of sound. A detailed discussion of the compressibility constraint in conjunction with alternate, multiple-relaxation-time (MRT) forms of the collision operator [14], can be found in [15].

Non-slip boundaries in the LBM can be handled using the bounce-back condition, which reflects the particle distribution functions arriving at a boundary node back toward their incident direction (i.e. 180° transformation). The straightforward and local nature of the bounce-back operator has resulted in its widespread use, despite well known issues related to spurious slip velocities [16] and variability in the apparent location of the boundary [17]. A range of velocity and pressure boundary implementations [16,18] is available in the LBM but neither is required in this study.

The method of Strack and Cook [19] is employed for the inclusion of fluid body forces, although a number of other implementations are available. In this approach a post-collision operator is included in the LBE to modify the momentum of the particle distribution functions such that Equation 1 becomes,

$$f_i(\mathbf{x}+\mathbf{c}_i\Delta t, t+\Delta t) = f_i(\mathbf{x},t) - \frac{\Delta t}{\tau}(f_i(\mathbf{x},t) - f_i^{eq}(\mathbf{x},t)) + A\mathbf{G}\cdot\mathbf{c}_i, \quad (9)$$

with $\mathbf{G}$ the fluid acceleration $[m/s^2]$. The coefficient, A, ensures mass conservation and for the $D3Q15$ lattice it is defined as $A = 1/10c^2$.

2.2 The discrete element method

The discrete element method has emerged as a powerful tool for the simulation of discontinuous problems in both science and engineering. As a particle-based method it can be used to model an assemblage of distinct particles (e.g. the flow of a pile of sand), discretise a fundamentally granular continuum (e.g. the loading of a sandstone specimen), or perform both at the same time (e.g. continuum-to-discrete fracture). Due to the presence of densely-packed particles subject to dynamic loads, the DEM is the logical choice for modelling the movement and interaction of suspended particles in this study.

The main algorithmic steps performed for each discrete element at each time step in the DEM include global spatial search for contact detection, local contact resolution, the calculation and summation of applied forces (e.g. contact, hydrodynamic, electromagnetic), and the integration of particle velocities and positions.

Typically, the most significant computational component of a DEM simulation is the contact search and in order to optimise this process a range of search algorithms have been defined [20]. This optimisation is considerably nuanced, with factors such as particle velocity, particle size distribution, packing density, and computational hardware all influencing the performance of the chosen algorithm [11]. Here, a *no binary search* (NBS) algorithm [21] is employed.

Once a list of potential contacts has been assembled by the search algorithm, contact resolution and force calculation are undertaken using a soft contact model. This relates the the normal, F_n, and tangential, F_t, contact forces between elements to the small, permissible overlap, δ, between their boundaries. In the normal direction this model can be generalised as,

$$F_n = \alpha k_n {\delta_n}^m, \quad (10)$$

in which k_n is the normal contact stiffness, α is a constant, and m is a parameter which facilitates a nonlinear relationship between overlap and force (e.g. $m \neq 1$ for a power law model). For the case of contacting spheres the overlap, δ, is calculated as,

$$\delta = |\mathbf{d}_1 - \mathbf{d}_2| - r_1 - r_2, \quad (11)$$

where $\mathbf{d}_i$ and r_i are the position vector and radius of particle i, respectively.

Similarly, the tangential contact force (excluding friction) is calculated as,

$$F_t = k_t {\mathbf{u}_t}^e, \quad (12)$$

in which k_t is the tangential contact stiffness, $\mathbf{u}_t$ is the relative tangential displacement between the contacting elements, and e denotes the *elastic* component of tangential contact. Full details of the Coulomb friction implementation can be found in [22].

After taking into account the mechanical DEM forces, the hydrodynamic LBM forces, and additional forces due to body forces, Reynolds lubrication or electromagnetic interaction, the velocity and position of each element is updated using a velocity Verlet integration scheme with a quaternion-based approach [23] for the rotational degrees of freedom. The explicit time step for integration is governed using a factored Courant-Friedrichs-Lewy condition,

$$\Delta t_{DEM} = \lambda\sqrt{|\frac{m}{k_n}|_{min}}, \quad (13)$$

in which λ is a constant (typically ~ 0.1) and $|m/k_n|_{min}$ represents the minimum combination of mass, m, and normal contact stiffness for all particles.

2.3 Hydrodynamic coupling of the LBM and DEM

A number of approaches have been proposed for the hydrodynamic coupling of moving obstacles with the LBM. These include the link-wise bounce-back method [1,2] and its many subsequent evolutions [24,17,25] and *dry* coupling methods [26]. Here, an immersed moving boundary (IMB) scheme [27,3] has been employed with a modification [28] which facilitates the coupling of multiple solid obstacles at a single LBM node, as shown in Figure 2, along with particles which are of the order of the lattice spacing in size. This sub-grid-scale condition addresses the momentum discontinuity of binary bounce back schemes and provides reasonable accuracy for obstacles mapped at low resolution.

In the IMB method the lattice Boltzmann equation is modified to include an additional collision operator, Ω^s_{id},

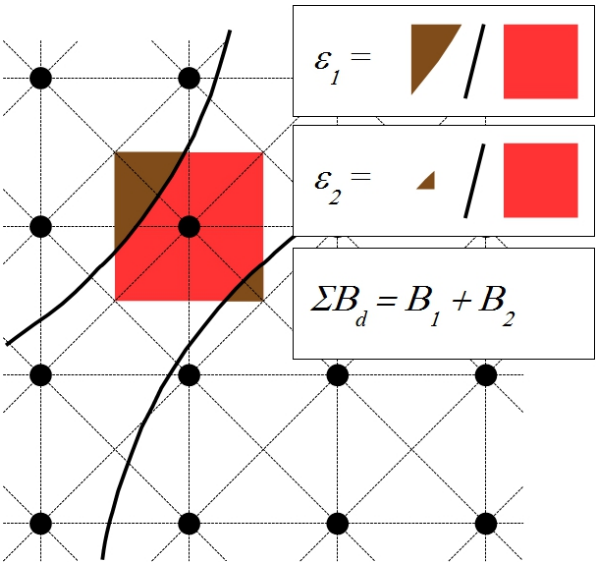

Fig. 2 A schematic representation of the calculation of the total solid fraction at an LBM node using the modified IMB method [28].

$$f_i(\mathbf{x}+\mathbf{c}_i\Delta t, t+\Delta t) = f_i(\mathbf{x},t) - \frac{\Delta t}{\tau}\left[1-\sum B_d\right](f_i(\mathbf{x},t) - f_i^{eq}(\mathbf{x},t)) + \sum B_d \Omega_{id}^s + \left[1-\sum B_d\right] A\mathbf{G}\cdot\mathbf{c}_i, \quad (14)$$

in which B_d is the weighting function for each obstacle, d, interacting with a node. This weighting is calculated using the local solid fraction, ε_d, of that obstacle at an LBM node (see Figure 2) and can be defined simply as the obstacles solid fraction,

$$B_d = \varepsilon_d, \quad (15)$$

or as a function of the solid fraction and the relaxation parameter,

$$B_d = \frac{\varepsilon_d(\tau - 1/2)}{(1-\varepsilon_d) + (\tau - 1/2)}. \quad (16)$$

A number of forms of the IMB collision operator have been proposed and these are summarised in [10]. Here, a definition based on bounce back of the nonequilibrium (NBB) function [27] is used,

$$\Omega_{id}^s = f_{-i}(\mathbf{x},t) - f_i(\mathbf{x},t) + f_i{}^{eq}(\rho,\mathbf{u}_s) - f_{-i}{}^{eq}(\rho,\mathbf{u}) \quad (17)$$

in which $\mathbf{u}_s$ is the weighted average of the velocity of the obstacles, and -i is used to denote the distribution function having the opposite direction to i.

Other forms of the IMB collision operator include a superposition (SP) operator [27],

$$\Omega_{id}^s = f_i{}^{eq}(\rho,\mathbf{u}_s) - f_i(\mathbf{x},t) + \left[1-\frac{\Delta t}{\tau}\right][f_i(\mathbf{x},t) - f_i{}^{eq}(\rho,\mathbf{u}_s)], \quad (18)$$

and a modification [29] of Equation 17,

$$\Omega_{id}^s = f_{-i}(\mathbf{x},t) - f_i(\mathbf{x},t) + f_i{}^{eq}(\rho,\mathbf{u}_s) - f_{-i}{}^{eq}(\rho,\mathbf{u}_s) \quad (19)$$

which is best suited to stationary obstacles (HBB), and therefore not relevant to this study.

In the IMB a number of combinations of collision operator and weighting function are possible. Once implemented at a node covered by an obstacle(s), the combined effect of, for example, Equations 14, 16 and 17 is to relax the particle distribution functions towards the equilibrium functions corresponding to the obstacles' rigid body motion. In this way, the no-slip condition is enforced and momentum of the background fluid is altered. To ensure conservation, equal and opposite momentum must be applied to the obstacle and this gives rise to the total hydrodynamic drag, $\mathbf{F}_f$, on an obstacle,

$$\mathbf{F}_f = \frac{\Delta x^2}{\Delta t}\sum_n \left(\sum B_d\right)_n \left(\sum_i \Omega_{id}^s \mathbf{c}_i\right), \quad (20)$$

where n represents all the nodes that map an obstacle to the lattice. Similarly, the hydrodynamic torque, $\mathbf{T}_f$, can be calculated,

$$\mathbf{T}_f = \frac{\Delta x^2}{\Delta t}\sum_n \left[(\mathbf{x}_n - \mathbf{x}_s) \times \left(\sum B_d\right)_n \sum_i \Omega_{id}^s \mathbf{c}_i\right], \quad (21)$$

where $\mathbf{x}_s$ is the centroid of the obstacle and $\mathbf{x}_n$ is the position of the node.

It is widely accepted [30] that, as presented, LBM-DEM modelling does not capture the details of lubrication effects as the distance between contacting solids vanishes. In spite of this, treatment of this limitation has received little attention in the literature. One approach [31] uses local grid spacing adjustments to try and capture lubrication forces, with limited success. Another [32] introduces phenomenological expressions for lubrication forces and an implicit solution strategy to capture this behaviour between spheres. However, due to the non-colloidal nature of the suspensions analysed, neither lubrication force model was included in this study.

2.4 Numerical Modelling of Charged Particles in Electromagnetic Fields

In the literature concerning the study of electromagnetic excitation of particles (which may or may not be in suspension) two different variations of interaction are common. The first, and the one utilised for this study, is the particles carrying a charge and thus interacting with the electromagnetic field via the Lorentz force equation [33–35]. The second, is to model particles of a magnetisable material that, upon application of an electromagnetic field, experiences a force between particles due to magnetic dipole interactions [36–39].

The fundamental relations that govern the behaviour of a charged particle within an electromagnetic field are widely available in elementary texts [40,41]. The main results utilised in this study are summarised as follows.

The force acting on a charged particle from an electromagnetic field is determined by the Lorentz equation,

$$\mathbf{F} = q(\mathbf{E} + \mathbf{u}_p \times \mathbf{B}), \tag{22}$$

in which $\mathbf{F}$ is the force on the particle $[N]$, q is the charge of the particles $[C]$, $\mathbf{u}_p$ is the particle velocity $[m/s]$, $\mathbf{E}$ is the electric field acting on the particle $[N/C]$ and $\mathbf{B}$ is the magnetic field $[T]$.

By virtue of the cross product, the velocity and magnetic fields will combine to produce a force acting perpendicular to both, which will only change the direction of a particle's motion rather than accelerating or decelerating it.

Electric Field Owing to the existence of the individual point charges, the simulations undertaken in this investigation will exhibit some form of electric field. This was considered in addition to any numerically applied field. The field for a single particle is described by Coulomb's law, and is additive for multiple particles,

$$\mathbf{E} = \frac{kq}{r^2}\hat{\mathbf{r}}, \tag{23}$$

in which k is a constant of value $9.0 \times 10^9\, Nm^2/C^2$, r is the distance from the centre of the particle to another particle $[m]$ and $\hat{\mathbf{r}}$ is a unit vector in this direction.

Magnetic field A moving charge will also produce a magnetic field around it according to the Biot-Savart law. This can be thought of as the magnetic field analogue to the Coulomb's law electric field. The magnetic field surrounding a moving charge is given as [42],

$$\mathbf{B} = \frac{\mu_0}{4\pi}\frac{q\mathbf{u}_r \times \hat{\mathbf{r}}}{r^2}, \tag{24}$$

where μ_0 is a permeability constant with value $4\pi \times 10^{-7} Tm/A$, and $\mathbf{u}_r$ is the relative velocity between the particle creating the field and the particle on which it is acting.

In Equations 23 and 24 the distance to the point of interest is taken from the centre of the spherical particles under consideration. The electric field aspect of this is a practical application of Gauss' law [41]. This relation implies that, within a uniformly charged sphere, the field strength grows linearly with the distance from the centre of the sphere. Outside the sphere the field decays proportionally to r^{-2} in accordance with Equation 23. The same behaviour will be assumed for magnetic interaction applied with Equation 24.

Electromagnetic suspensions For the calculation of hydrodynamic forces both Pappas and Klingenberg [37] and Lindner et al. [39] use a Stokes drag term that is included in the DEM calculation. In contrast, Han et al. [36] use an LBM-DEM framework similar to that described in Sections 2.1 to 2.3. Although more computationally expensive, this technique does allow analysis of systems where Stokes drag is not valid.

In their study of the Brownian dynamics of charged particles, Hou et al. [33] compare a number of integration schemes, namely explicit Euler-like and Beeman-like (a similar system to the Verlet technique described in Section 2.2) algorithms and a predictor-corrector Gear-like algorithm. Upon comparison to analytical solutions for a three-dimensional Brownian harmonic oscillator they found that the predictor-corrector method provided the best accuracy and stability overall but for intermediate damping the Beeman-like formulation was best.

Recent works by Zohdi [43–47] and Mukherjee et al. [48,49] consider the behaviour of a charged particle within an electromagnetic field. In these, a similar array of fields and forces to the current work are investigated. In particular the use of the Lorentz force equation for the application of externally generated electromagnetic fields on point charges is investigated. It should be noted that in these studies the effect of inter-particle interactions such as Coulomb's law may be included either explicitly or in an empirical near-field force term [43–46] but is sometimes neglected [47–49].

In [47,49] the behaviour of a charged particle subject to electromagnetic excitation within a fluid is modelled through a DEM-only style of particle force application. The electromagnetic forces are ultimately applied to each particle via the Lorentz force equation in

a similar fashion to the approach used in this study. The hydrodynamic forces, however, are calculated via a drag coefficient rather than being resolved using the LBM. Due to the high solid volume fraction of suspensions investigated, the LBM approach was deemed more appropriate in this study. The description of fluid mechanics in [47] has been dealt with using a FD solver to discretize the Navier-Stokes equations, whilst in [49] a steady-state flow solution fixes the fluid behaviour. Similarly, in [43,46,48] a DEM-style approach is used for the application of the electromagnetic forces to the particles but instead examines contexts in which there is no surrounding fluid medium.

3 Validation and Verification of the LBM-DEM Model

Based on the theoretical relations discussed in Section 2.4, a strategy was developed to numerically determine the interaction of charged particles with both each other and an external electromagnetic field. The major assumptions that were made in the development of this model were:

i. Electric and magnetic fields each oscillate in a steady, sinusoidal fashion;

ii. Electric and magnetic fields possess uniform strength throughout the test domain at any given time;

iii. Magnetic fields induced by individual particle motion (Biot-Savart interactions between particles) are negligible in comparison to the Coulomb's law interactions and the applied electric field;

iv. Particles are treated as point charges with constant physical properties;

v. Behaviour observed in the test domain is representative of the entire system;

vi. DEM and LBM solution parameters are kept constant between tests.

It was noted by Zohdi [43] that the magnetic fields generated by Biot-Savart interactions between the charged particles were negligible due to the small velocities of the particles involved in that study. As the particle velocities in this study are much smaller again than those used in [43] the assumption to neglect these effects can be safely made here.

The correct application of external electromagnetic fields, Coulomb's law particle interactions and particle contacts with bounding walls were verified by comparing the output data from the numerical model to those computed by the analytical equations presented in Section 2. These were found to be in agreement up to the order of the significant figures of the output data.

Behaviour of the electromagnetic LBM-DEM model was investigated by performing trials with two test spaces. The first was comprised of a single particle located at the centre of a closed, cubic LBM-DEM domain, while the second incorporated a collection of five particles located within the same domain. Numerous combinations of field strength, field frequency and particle charge were applied to each model. To investigate the model's sensitivity to these parameters, a number of outputs were examined to provide a quantitative basis for investigations. These included particle position and velocity in the direction of the applied field, and the hydrodynamic drag acting on a particle in the direction of the applied field.

The LBM-DEM solution parameters, namely time step, grid spacing and relaxation parameter, were kept constant in these tests to isolate the effects of varying electromagnetic parameters. Simulations were run for the equivalent of five field cycles as this was observed to be long enough for transient effects to have dissipated.

In the validation tests it was noted that a particle charge of $\mathcal{O}(10^{-12} \sim 10^{-18}C)$ was required to avoid the force arising from the Coulomb's law electric field dominating the force due to the applied field. This was identified to be due to the large value of k in Coulomb's law and the separation of particles being typically much less than one millimetre.

In these tests it quickly became apparent that the magnetic field had a negligible impact on particle motion. For the parameters used in this investigation, the magnetic field needed to be at least one order of magnitude greater than the electric field to induce a force of similar magnitude on a particle. This corresponds to a magnetic field with an amplitude of at least 10^7T, which is several orders of magnitude greater than anything yet created on Earth. Given these observations it was decided to neglect magnetic fields from further testing.

3.1 Single particle testing

Figures 3(a) and 3(b) illustrate the behaviour of a single particle in a fluid at various levels of charge. These values were chosen, based on preliminary validation testing, so that Coulomb's law interactions did not dominate the applied electric field and negate the desired oscillation of particles. The possible effect of Coulomb's

law interactions changing the behaviour seen due to the external field has been noted elsewhere [48]. In a similar manner to the current work, Mukherjee and Zohdi [48] implemented scenarios in which the forces from the external field would generally dominate those from Coulomb based interactions. All tests in these figures occurred at a field oscillation frequency of $50Hz$. A similar range of tests was conducted with particle charge fixed at $10^{-15}C$ over a range of field oscillation frequencies, the results of which are given in Figures 3(c) and 3(d). Trials for a particle with a charge of 10^{-12} C at field amplitudes of $10^{9}N/C$, $10^{10}N/C$ and $10^{12}N/C$, as well as a charge of $10^{-15}C$ in conjunction with a field of $10^{12}N/C$, were unable to be completed due to the particle velocity creating model instability. This indicated an upper bound of solver stability based on the magnitude of the electromagnetic force acting on a particle.

The maximum electromagnetic force acting on a charged particle in the electric field is given by the product of particle charge and applied field amplitude. At constant values of this product near identical results for both particle motion and velocity amplitude occurred. This indicates that predictions of behaviour in further testing can be made by only looking at the maximal electromagnetic force acting on a particle rather than performing several cases with various charge and field properties. Also implied is some freedom of choice of charge and field values to become physically reasonable so long as a necessary product is maintained. However, this assumption will collapse at large values of charge when the field acting on a particle due to Coulomb's law will dominate the applied field.

The steady state response of a single particle velocity and oscillation amplitude can be seen to vary directly with its charge. When viewed on logarithmic axes the variation of displacement and velocity is linear, most clearly evidenced by the trials with a charge of 10^{-18} C (see Figures 3(a) and 3(b)). The trials with larger charges were truncated from a linear trajectory at higher field amplitudes as the particle approached and collided with the surrounding boundaries. To overcome the hydrodynamic drag on a particle and move it with a displacement amplitude of at least 10% of its radius, a force of at least $10^{-6}N$ was required.

The gradient of this linear behaviour is dependent on the physical and electromagnetic properties of the particle, the viscosity of the fluid and the integration scheme used to determine velocity and position. The relationship of these factors to the gradient has not been determined here as focus has been placed on the trends in the model. This would make an ideal candidate for further work in a more analytical investigation of particle behaviour.

Given the sinusoidal field that was applied to the system, the consistent growth of particle oscillation amplitude with frequency (see Figure 3(c)) can be seen to correspond to the amount of time that a force is acting on a particle. In the $25Hz$ tests the electric field, and thus force on a particle, is acting in the same direction for $0.02s$ at a time (i.e. half of one oscillation period). When a $100Hz$ field is applied this reduces to only $0.005s$. Intuitively, the longer a particle is forced in a given direction the greater the displacement that occurs. The convergence of the particle amplitudes towards a single value when the field amplitude is at a value of $10^{10}N/C$ in Figure 3(c) is due to the particle colliding with the domain boundaries.

3.2 Multiple particle testing

A similar range of tests was performed on a five particle array to investigate the impact of particle interactions. The displacement and velocity amplitude results for both charge and frequency variation are presented in Figure 4. The amplitudes given in these plots were found after averaging the individual particle behaviour for each trial.

When multiple particles were simulated many similar observations to those made for single particle behaviour could be made. When viewed on a logarithmic scale, linear growth of steady state displacement and velocity amplitudes is again generally observed (see Figure 4). When the charge was $10^{-18}C$, however, the amplitude of both these measures was constant for field amplitudes at and below $10^{8}N/C$. In these cases the applied electric force was too small to cause a net effect on the averaged behaviour of the five interacting particles.

The position and velocity variation of the combined particle group varied in a similar manner with frequency to the single particle tests. The observations at each electric field amplitude were, however, less tightly clustered than the single particle case. This is believed to be due to the averaging of particle behaviour to gain a single quantitative output. It is also believed that the initial individual particle locations within the domain have an impact on this behaviour. A force of $10^{-6}N$ was again necessary to overcome the hydrodynamic drag on the particles and move the average location roughly 10% of a single particle radius.

The convergence of the particle oscillation amplitudes at higher applied field amplitudes in Figure 4(c) is due to particles colliding with the domain boundaries. At smaller applied amplitudes it is due to the applied electromagnetic force being unable to overcome

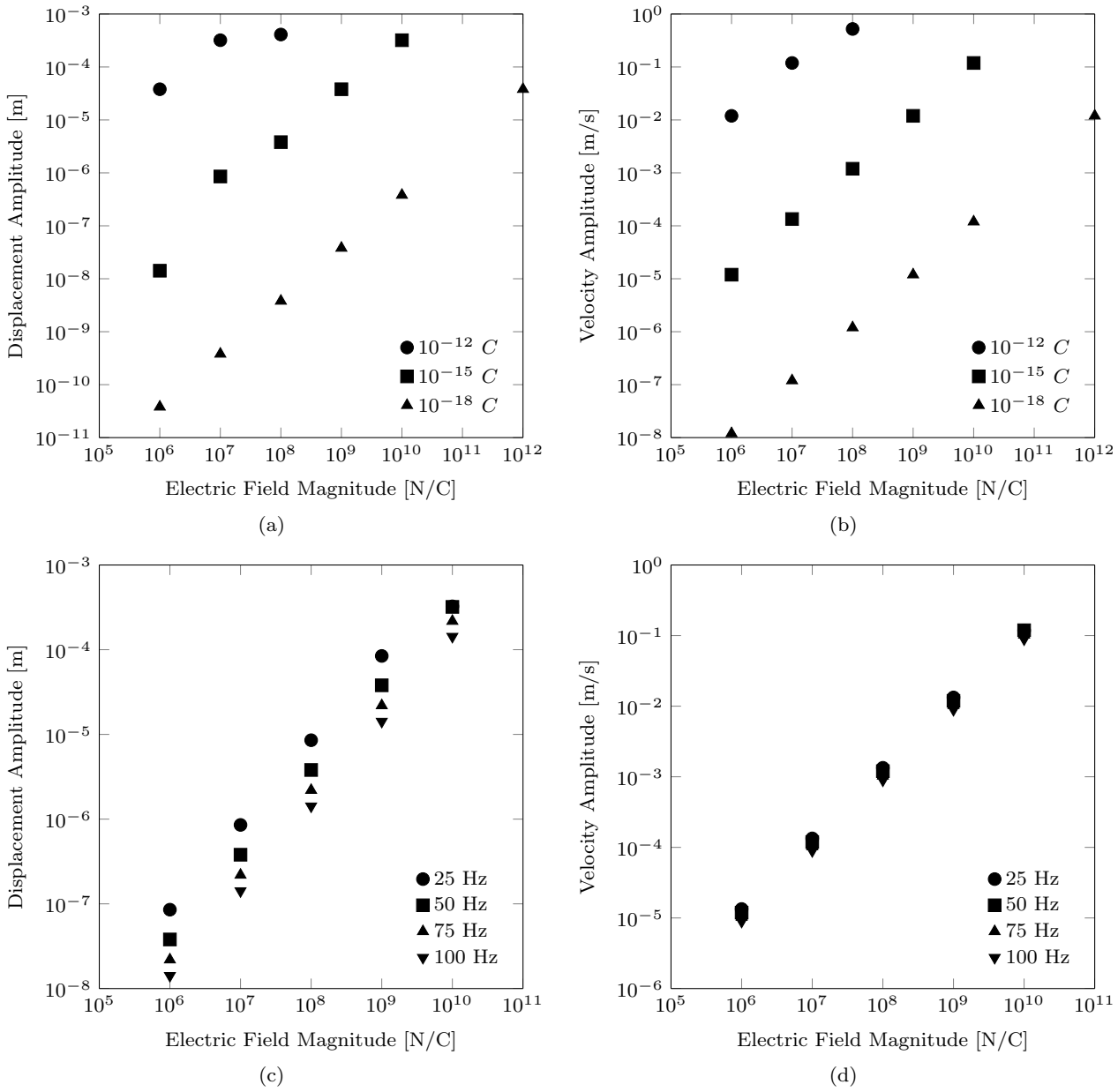

Fig. 3 Steady state amplitudes of displacement and velocity of a single particle, including (a) displacement and (b) velocity due to an electric field oscillating at a fixed frequency of $50Hz$ whilst varying the charge of the particle and the amplitude of the applied electric field, along with (c) displacement and (d) velocity due to an electric field oscillating with varying frequency and amplitude and a fixed particle charge of $10^{-15}C$.

the fluid drag acting on the particles to enable the average motion of the collection to vary between tests.

From the single and five particle tests the following features of the developed model could be identified:

i. For feasible charge values ($10^{-12} \sim 10^{-18}C$) the particle motion was almost identical for tests with a constant product of charge and field amplitude;
ii. To overcome the hydrodynamic drag of the suspending fluid it was noted that a force of at least $10^{-6}N$ acting on a particle of the assumed properties was necessary;
iii. Greater motion and acceleration of particles was seen for lower frequency trials, due to the longer period of force application in the same direction;
iv. When placed on a logarithmic scale the variation of particle behaviour (either the oscillation amplitude of displacement or velocity) was essentially linear when either particle charge or oscillation frequency was varied. When this did not occur it meant that

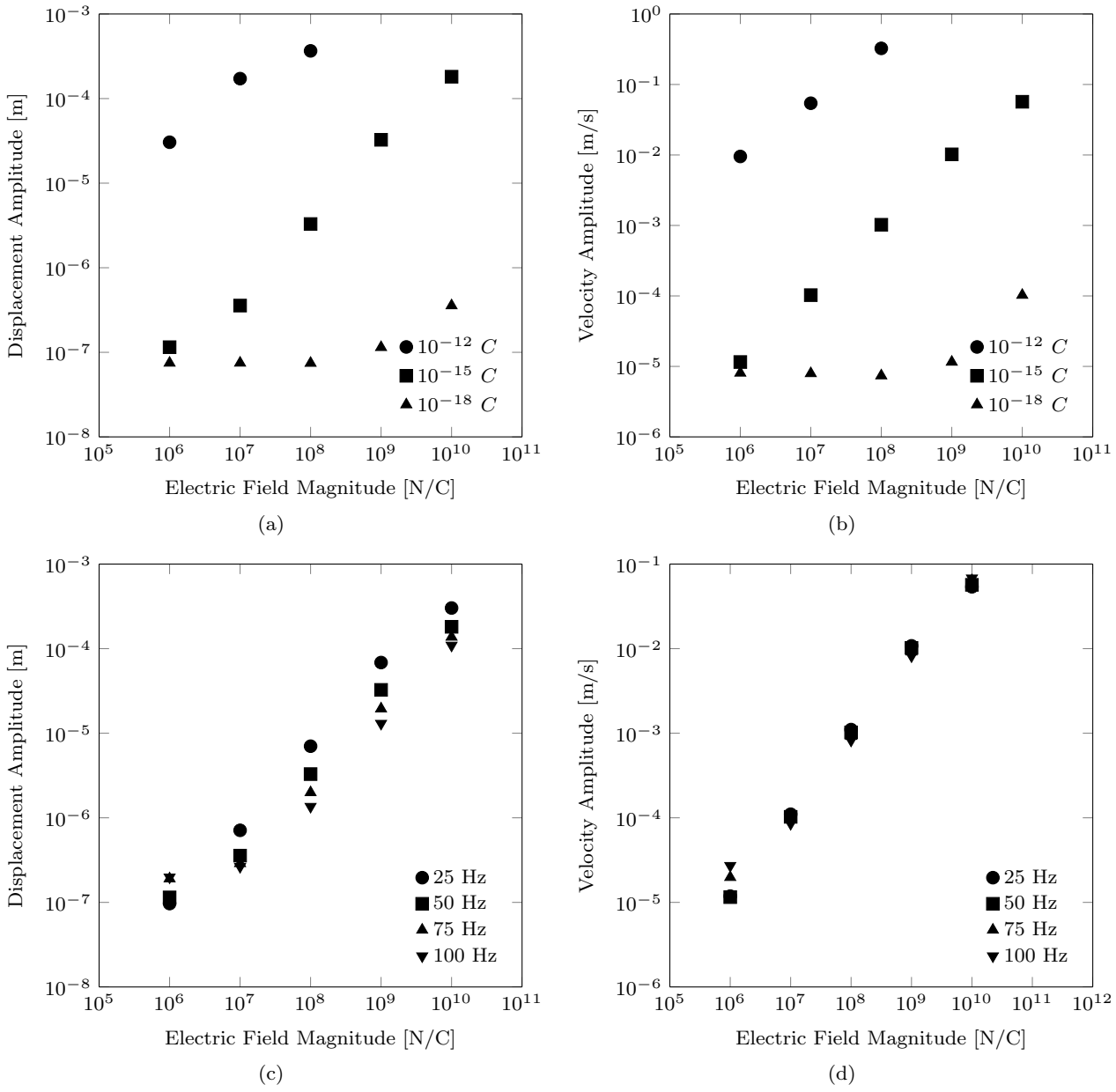

Fig. 4 Averaged steady state amplitudes of displacement and velocity of a five particle cluster, including (a) displacement and (b) velocity due to an electric field oscillating at a fixed frequency of $50Hz$ whilst varying the charge of the particles and the amplitude of the applied electric field, along with (c) displacement and (d) velocity due to an electric field oscillating with varying frequency and amplitude and a fixed particle charge of $10^{-15}C$.

either the particles were colliding with the domain boundaries or the electric force on the particles was not sufficient to overcome fluid drag.

4 Numerical Illustration: Electromagnetic excitation of non-colloidal suspensions in hydraulic fractures

Unconventional oil and gas resources, such as those associated with shale formations and coal seams, have rapidly become an important component of the world energy supply [50]. To help meet future energy requirements, the recovery of these low porosity-permeability resources needs to be maximised. To this end, the well completion process known as hydraulic fracturing is commonly used to stimulate the flow of gas from a reservoir. The modelling and development of minimally invasive techniques that enable the tracking of hydraulic fractures and fracture fluids within a reservoir would allow the resource extraction process to be optimised for

an individual site, providing both environmental and economic benefits.

Hydraulic fracturing involves pumping a complex particle suspension (fracture fluid) into an oil or gas bearing reservoir. The pressure from the fluid injection causes fractures to occur within the formation which are then filled by the suspension as the process progresses. When the fluid phase of the suspension is removed, the solid phase (called proppant) remains to ensure the fractures are supported to allow the flow of oil or gas through the created, high-permeability pathways [51].

One of the challenges associated with hydraulic fracturing is that it is regularly employed in formations more than one kilometre below ground level. As such the propagation behaviour of fractures through a reservoir can be difficult to determine. Knowledge of the location of a fracture would allow its progress to be modified to maximise performance.

One existing approach used to track hydraulic fractures is microseismic monitoring. This records the physical phenomena caused by fracture propagation acting like a microearthquake [52]. As the fracture opens it propagates a primary (or compression) wave and a shearing wave (P- and S- waves, respectively) through the surrounding medium. Determining the arrival times of the P- and S- waves at acoustic receivers known as geophones allows estimation of the location of the fracture relative to these points. These geophones may be located either on the ground surface or within a borehole [53, 54].

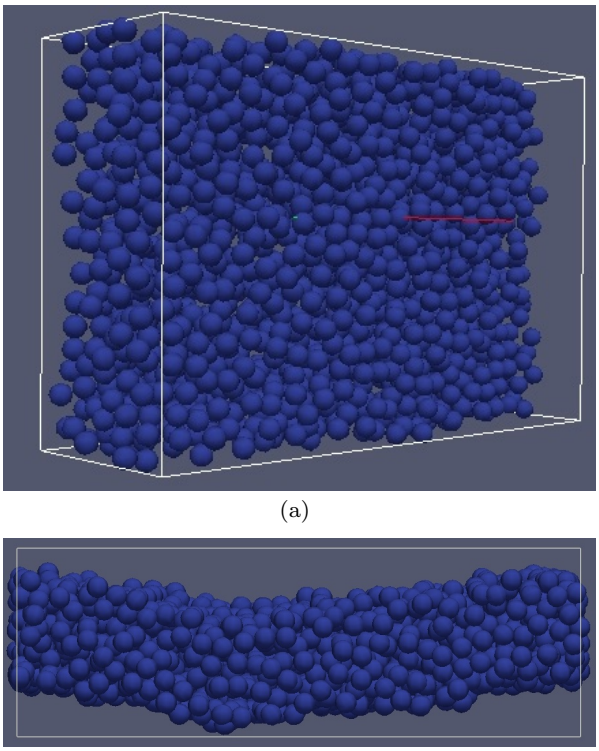

(a)

(b)

Fig. 5 Rendering of an (a) isometric view and (b) top view of the fracture model with a 35% SVF particle pack. The white box represents the outer bound of the surrounding fluid domain.

4.1 Hypothesis and modelling strategy

The objective of this numerical illustration is to explore the possibility of using electromagnetically excited fracture fluids to aid the microseismic tracking of hydraulic fractures. In this scenario an applied field induces motion of the charged particles, causing them to repeatedly collide with the fracture walls. The acoustic signal that is created within the surrounding rock by this process would then be analysed by surface or down-hole geophones to infer knowledge of the fracture's location, orientation and propagation behaviour.

From Section 3, combinations of parameters that were numerically stable and could potentially yield a suitable output signal were identified. These parameter sets were tested against each other on two fracture models with solid volume fractions (SVF) of 10% and 35%, respectively, in order to compare behaviour. These fracture models approximated a rectangular prism with irregular walls for the upper and lower surfaces and periodic boundary conditions for the remaining sides to replicate a larger fracture, as shown in Figure 5. A body force was applied to the fluid to model the flow of the proppant through the fracture.

The main output of information from these trials were time traces of the collision forces acting on the walls of the models, as shown in Figure 6. Two separate analyses of this data occurred, both of which were extrapolated to a unit area. Firstly, an average of this data over the test time was found. As the contact force from the particles is measured over the entire area of the wall this corresponds to a pressure measurement. Secondly the output data was numerically integrated in time to determine the impulse imparted to the wall. This data was finally analysed to simulate the action of a geophone at a given distance from a fracture. Such recording devices convert the velocity of vibration to a signal voltage. The magnitude of wall vibration velocity was calculated in two ways, as discussed below. It must be emphasised that both of these techniques are based on basic principles and by their nature are considered approximate. Development of one or both of them would be required for the continuation of work derived from this study.

Vibration Estimate I Assume that the displacement of a unit length cubic volume varied in a sinusoidal fashion with frequency matching the applied field. The amplitude of displacement was estimated using the peak pressure exerted on the wall by particle collisions and the Young's Modulus of the wall material,

$$\Delta = \frac{P}{E}, \tag{25}$$

in which Δ is the relative displacement of the unit length cubic volume [-], P is the peak pressure exerted on the wall $[Pa]$, and E is the Young's Modulus of the surrounding rock $[Pa]$. The magnitude of velocity is then the product of frequency and displacement magnitude.

Vibration Estimate II Assume that the calculated impulse over a given cycle accelerates a rigid, unit-length, cubic volume of surrounding material between the fracture and the recording device location. The computed velocity can be calculated as,

$$I = m(V_2 - V_1), \tag{26}$$

in which I is the impulse imparted on the wall over a single cycle $[Pa.s]$, m is the mass of a unit length of cubic volume $[kg]$ and V is the initial (state 1) or final (state 2) velocity of the volume $[m/s]$. The volume is assumed to initially be at rest.

This *recorded data* was compared to literature values for the background noise of a hydraulic fracturing operation at the frequency of oscillation to determine the signal-to-noise ratio (SNR). The practicality of the demands of detecting a given SNR and using the applied field were then used to judge the feasibility of electromagnetic particle stimulation as a means of hydraulic fracture tracking. Kim and Lee [55] studied how vibrations are damped, as a function of distance, by the ground (both on the surface and underground) for a variety of noise sources. The recorded data in this study examined vibrations below $100Hz$ frequency. They found good agreement with the theoretical attenuation model,

$$w_2 = w_1(\frac{r_1}{r_2})^n e^{-\alpha(r_2 - r_1)}, \tag{27}$$

in which w is the vibration amplitude $[m]$ a distance r $[m]$ from a noise source, n is a geometric damping coefficient which varies depending on the type of noise source present, and α is a material damping coefficient that is governed by the ground type through which the vibration is travelling and the frequency of the vibration. Classifying a fracture as a buried line source of noise creating body waves through the soil would require $n = 0.5$. For simplicity there was assumed to be no ground damping (i.e. $\alpha = 0$).

Table 1 Wall collision data for SVF = 10%.

Field Amplitude [N/C]		10^{10}	10^{10}	10^{10}
Particle Charge [C]		10^{-15}	10^{-15}	10^{-15}
Field Frequency [Hz]		25	50	75
Average Wall Pressure [Pa]	Upper	0.108	0.001	0
	Upper Trimmed	0.427	0.029	0
	Lower	-0.677	-0.763	-0.977
	Lower Trimmed	-1.477	-1.268	-1.231
Impulse per Area [Pa.s]	Upper	0.022	0	0
	Lower	-0.136	-0.076	-0.065

Table 2 Wall collision data for SVF = 35%.

Field Amplitude [N/C]		10^{10}	10^{10}	10^{10}
Particle Charge [C]		10^{-15}	10^{-15}	10^{-15}
Field Frequency [Hz]		25	50	75
Average Wall Pressure [Pa]	Upper	0.427	0.080	0
	Upper Trimmed	1.173	0.268	0
	Lower	-4.122	-4.838	-5.614
	Lower Trimmed	-5.725	-5.079	-5.685
Impulse per Area [Pa.s]	Upper	0.086	0.008	0
	Lower	-0.825	-0.484	-0.375

4.2 Modelling results and discussion

Three measures of particle impacts against the walls were generated from the data output over each trial of approximately five full oscillations of the applied field. These were the average wall pressure experienced, the average pressure that occurred only when particles are in contact with the wall (*trimmed* values, i.e. the values with zero contact force are removed), and the impulse imparted by the particles on the wall. These were calculated for both the upper and lower walls in the models. Tables 1 and 2 present the calculated values of these measures for both the 10% and 35% SVF models. The pressure values for the lower wall are negative due to its orientation within the domain. Particles were moving in the negative axis direction when they collide with the lower wall hence the impact force imparted on the wall is also in the negative direction.

Table 3 Scaling factors of wall collision data from SVF = 10% to SVF = 35%.

Field Amplitude [N/C]		10^{10}	10^{10}	10^{10}
Particle Charge [C]		10^{-15}	10^{-15}	10^{-15}
Field Frequency [Hz]		25	50	75
Average Wall Pressure [Pa]	Upper	3.97	54.1	0
	Upper Trimmed	2.75	9.63	0
	Lower	6.09	6.34	5.74
	Lower Trimmed	3.88	4.00	4.62
Impulse per Area [Pa.s]	Upper	3.97	54.1	0
	Lower	6.09	6.34	5.74

The pressure and impulse data presented in Tables 1 and 2 have been determined by scaling the output data from the physical model dimensions. Due to the particles not reaching the upper wall in some cases the lower wall data is the more reliable method of making a comparison between the two SVF cases. The wall pressure measurement can be used to estimate the steady state amplitude of vibration of the fracture wall per unit area based on wall stiffness in a linear spring model and Equation 25. The impulse figure is a measure of the amount of momentum transferred from the particles to the wall as a result of their collisions. Table 3 gives the factor of increase when the SVF is increased from 10% to 35%.

The main conclusion to be drawn from this table is that neither wall pressure nor impulse scale proportionately with SVF increase. The true relationship cannot be determined from the tests conducted as part of this investigation as only two SVF cases were available for this study. This behaviour presents an opportunity for further research. It is hypothesised, however, that the observed increase in average wall pressure and total impulse is a result of the higher SVF model having a more even distribution of particles throughout the fracture domain. This consequently means a greater number of particles are located against the fracture walls at a given point in time. This may not grow evenly with SVF due to the random packing distributions used to create the fracture models. It should also be noted that any increase in wall collision parameters with SVF would be limited by the case at which no more particles can be introduced into contact with the wall.

Traces of upper and lower wall pressure, along with the applied field, are shown in Figure 6 for a $50Hz$ trial. Note that the field line in this graph represents the relative value of the applied field at a given point in time. It is not scaled to the vertical axis and merely indicates when the field peaks and changes direction.

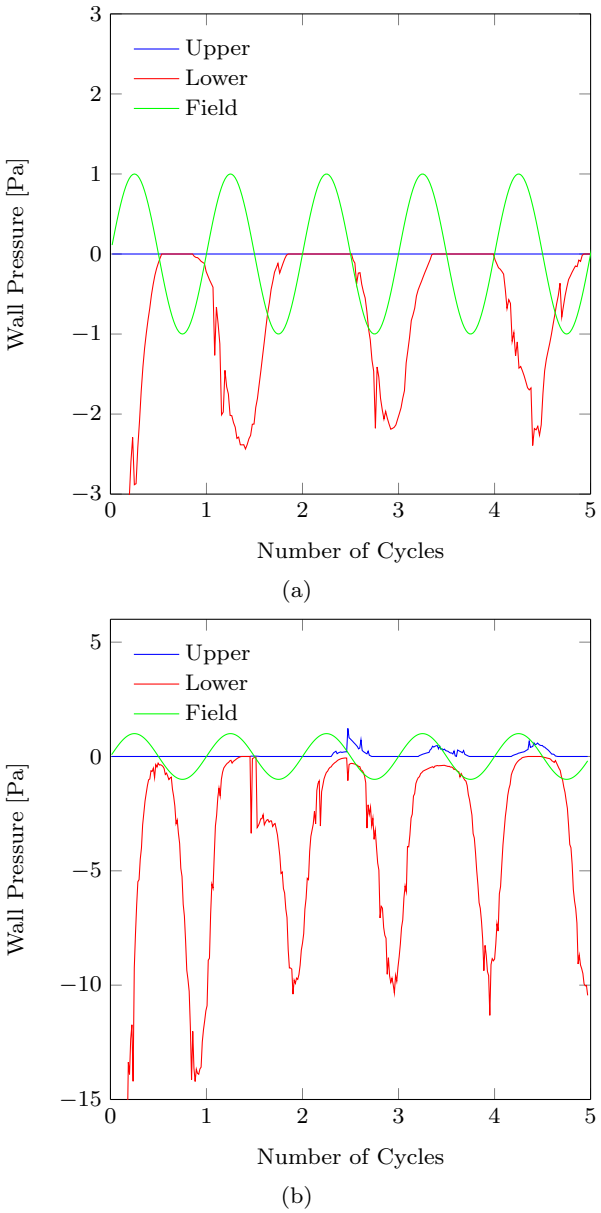

Fig. 6 Wall pressure and applied field traces for (a) 10% SVF and (b) 35% SVF.

In the fracture models, the initial packing distribution had some particles in contact with the lower wall. These particles were forced away from the wall in the initial few time steps of the calculation due to contact forces. The solver parameters that influenced hydrodynamic drag in these tests mean that it would take a significant amount of time for particles to not only separate from the wall but also reach the upper wall. This time frame was of a similar order to the time required for the field to change direction. These factors meant that a large pressure against the lower wall and a small pressure against the upper wall was observed.

The question that this numerical illustration is trying to answer is whether the acoustic signal generated by the collision of particles against a wall is sufficient to be used as a method for tracking hydraulic fractures. The means of generating the applied field and charged particles are not of primary concern, however these are discussed further below. Any stimulated vibration would be detected through the use of geophones that have been assumed to possess a sensitivity of $30V/m/s$.

For the first method of calculating the particle-induced ground vibrations it has been assumed that the displacement of the wall vibration is sinusoidal at the applied frequency of the field. The amplitude of the velocity is given by the product of the radian frequency of the field and the maximum displacement of the wall due to the contact pressure of the particles as calculated by a spring model. The Young's Modulus of the surrounding rock has been assumed to be an average value for shale [56]. In the second method, the amplitude of velocity is given by the impulse of a single cycle divided by the mass of the column of wall material between the fracture and the measurement location. The density of the wall has been assumed to be a standard value for shale.

In both cases the attenuation of the signal with distance was modelled using Equation 27 for distances of 50, 100, 150 and $200m$ from the fracture. No damping was used to calculate the vibration signal received at the fracture. These distances have been designated to act as an initial proof of concept of the proposed technique.

Feasibility of identifying a vibration signal has been estimated by calculating the SNR of the model outputs. A background noise level of $-28dB$ at $50Hz$ is assumed [52] to act at the geophone location. For the purposes of this investigation the reference level at which the noise and signals are compared has been assumed to be $0dB$. Taking this into account the SNR can be calculated as,

$$SNR(dB) = 10log(signal) + 28, \tag{28}$$

in which the *signal* is the estimated geophone voltage stimulated by the wall vibration.

Under these conditions the SNR at each SVF was found to change as shown in Figure 7 for the $50Hz$ trial. This frequency was chosen as the smaller amount of noise at this frequency gave it a better chance of creating a usable signal in comparison to the $25Hz$ trial despite having smaller pressure and impulse peaks. The results are similar for both calculation methods.

Song et al. [52] implemented a filtering technique that required a SNR of at least $6dB$ to discern an incoming signal. Neither method for estimating the acoustic signal generated by the proposed hydraulic fracture technique met this criterion at any SVF or distance combination. The values of SNR less than $0dB$ indicate the signal being dominated by the background noise.

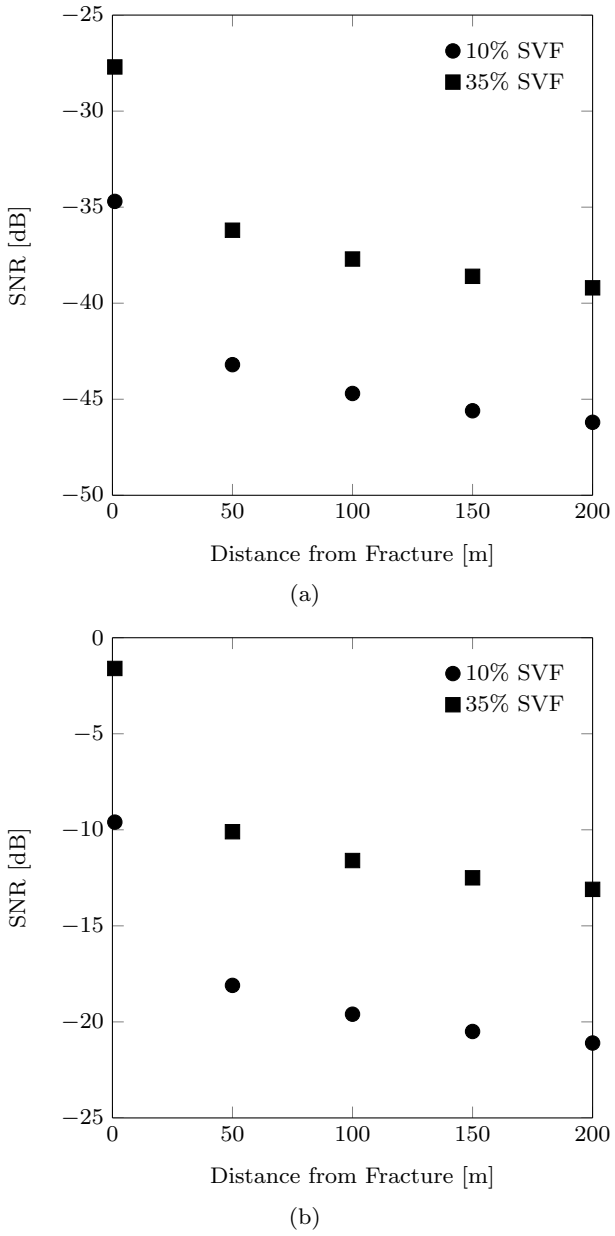

Fig. 7 Decay of SNR with distance from a fracture using (a) the wall pressure method and (b) impulse method.

There may be some benefit in further investigating the general principle of the proposed technique discussed here for situations where the distance between the vibration source and receiver is not as great, the background noise is less intrusive or the material through which generated signals travel is more conducive to its passage. Such scenarios could include monitoring of water mains or domestic plumbing and biological applica-

tions. The ability to control the motion of suspended particles would also be useful in these situations. Particle motion control would also have potential, more generally, in increasing the flow of suspensions in situations such as concrete pumping.

The difference in estimated signal between the two SNR calculation methods highlights the need to refine these approximate techniques if further investigations were to be carried out. However, for the purposes of this numerical illustration, both have been deemed sufficient. The electric field necessary to move the particles considered in this example are above those created in typical industrial applications and, indeed, well above the safe limits for human exposure. As was noted in Section 3, as long as the product of charge and field amplitude is constant the observed particle behaviour did not change appreciably for the values tested. Thus to reduce the field to safe limits the ability to endow particles with significantly greater charges than those used in the bulk of this study needs to be achieved. Doing this, however, would increase the repulsion between particles due to the Coulomb's law field created between them, altering the behaviour of the system from the trends observed here.

The reason for the unreasonably large electric or magnetic field that is necessary to move a particle within a fluid is significantly affected by the viscosity of the fluid and the size of the particles that have been investigated. Other works [36] achieve numerical particle motion with more reasonably sized electromagnetic fields by modelling particles that are approximately 100 times smaller than those under investigation here. The corresponding increase in hydrodynamic drag that needs to be overcome by the applied force necessitates the field amplitudes investigated. The model developed using charged particles and the Lorentz force equation also necessitates large fields due to the small charges being used.

5 Conclusion

This investigation has focused on the development of a numerical model that provides an explicit implementation of electromagnetic force interactions between charged particles within a suspension. The model utilises a coupled framework of the DEM (for the particle mechanics) and the LBM (for the fluid mechanics) to capture the behaviour of a particle suspension.

The numerical tests conducted investigated the action of an oscillating electric field acting on rigid, submillimetre spherical particles which possess a fixed charge. Magnetic field interactions were omitted after it was determined that the field necessary to move a particle within the test fluid was inordinately large. Electromagnetic interactions due to Coulomb's law and the Lorentz force equation were applied via DEM to the particles according to their charge values and the applied field. Validation testing of the model using specific particle interaction scenarios was used to check the formulation of the code and compare output data to theoretical results. The model was found to be accurate within the numerical rounding of the data output. The sensitivity of the model to variation of field amplitude, oscillation frequency and particle charge was then investigated through the application of an electric field to both single particle and a collection of five particles within a bounding box of DEM walls.

The developed model was then applied to two hydraulic fracture models with different particle SVFs to investigate the feasibility of using charged particles under electromagnetic excitation as a method for monitoring fracture growth. Particle collisions with both side walls were tracked at each time step during the application of the desired field for five field oscillations. In comparisons between these models it was noted that the pressure and impulse imparted by the collision did not necessarily grow proportionally with SVF but rather depended on the number of particles that were within an appropriate proximity to the wall. This may not grow proportionately with SVF due to the random particle distributions used to create the fracture models.

Using two approximate techniques, these outputs were converted to a likely signal recorded by a geophone at various distances from the fracture. These were compared to the typical background noise of a hydraulic fracturing location at the $50Hz$ frequency of interest to determine the SNR of the vibration generated at the fracture. This comparison found that even with a large electric field the acoustic signal created by such vibrations were dominated by background noise at the distances necessary for hydraulic fracture tracking. However, a number of physical contexts (where the fluid, solid, and distance properties are more favourable) have been identified as potential applications of this technique.

Acknowledgements Aspects of the hydrodynamic coupling of the LBM and DEM were presented in part at the 6^{th} International Conference on Discrete Element Methods (DEM6) in 2013.

References

1. A.J.C. Ladd, Journal of Fluid Mechanics **271**, 285 (1994)
2. A.J.C. Ladd, Journal of Fluid Mechanics **271**, 311 (1994)
3. B.K. Cook, D.R. Noble, J.R. Williams, Engineering Computations **21**(2/3/4), 151 (2004)

4. Y.T. Feng, K. Han, D.R.J. Owen, International Journal for Numerical Methods in Engineering **72**(9), 1111 (2007). URL http://dx.doi.org/10.1002/nme.2114
5. G.R. McNamara, G. Zanetti, Phys. Rev. Lett. **61**(20), 2332 (1988). URL http://link.aps.org/abstract/PRL/v61/p2332
6. S. Chen, G.D. Doolen, Annu. Rev. Fluid Mech. **30**(1), 329 (1998). URL http://dx.doi.org/10.1146/annurev.fluid.30.1.329
7. P.L. Bhatnagar, E.P. Gross, M. Krook, Phys. Rev. **94**(3), 511 (1954). URL http://link.aps.org/abstract/PR/v94/p511
8. H. Chen, S. Chen, W.H. Matthaeus, Phys. Rev. A **45**(8), R5339 (1992). URL http://link.aps.org/abstract/PRA/v45/pR5339
9. Y.H. Qian, D. D'Humieres, P. Lallemand, Europhys. Lett. **17**(6), 479 (1992)
10. D.R.J. Owen, C.R. Leonardi, Y.T. Feng, Int. J. Numer. Meth. Engng. **87**(1-5), 66 (2011)
11. R.S. Maier, R.S. Bernard, D.W. Grunau, Physics of Fluids **8**(7), 1788 (1996). URL http://link.aip.org/link/?PHF/8/1788/1
12. S. Hou, Q. Zou, S. Chen, G. Doolen, A.C. Cogley, J. Comput. Phys. **118**(2), 329 (1995). URL http://www.sciencedirect.com/science/article/B6WHY-45NJMV8-1G/2/1f980007815bebca21f65512bdaf9750
13. J.D. Sterling, S. Chen, Journal of Computational Physics **123**(1), 196 (1996). URL http://www.sciencedirect.com/science/article/B6WHY-45NJMH5-1Y/2/bf9430f70eddc2fac24d59d853fef518
14. P. Lallemand, L.S. Luo, Phys. Rev. E **61**(6), 6546 (2000). URL http://link.aps.org/abstract/PRE/v61/p6546
15. P.J. Dellar, Journal of Computational Physics **190**(2), 351 (2003). DOI http://dx.doi.org/10.1016/S0021-9991(03)00279-1. URL http://www.sciencedirect.com/science/article/pii/S0021999103002791
16. Q. Zou, X. He, Phys. Fluids **9**(6), 1591 (1997). URL http://link.aip.org/link/?PHF/9/1591/1
17. R. Verberg, A.J.C. Ladd, Physical Review E **65**(1), 1 (2001). URL http://link.aps.org/abstract/PRE/v65/e016701
18. J. Latt, B. Chopard, O. Malaspinas, M. Deville, A. Michler, Physical Review E **77**, 056703 (2008). DOI 10.1103/PhysRevE.77.056703. URL http://link.aps.org/doi/10.1103/PhysRevE.77.056703
19. O.E. Strack, B.K. Cook, Int. J. Numer. Meth. Fluids **55**(2), 103 (2007). URL http://dx.doi.org/10.1002/fld.1437
20. J. Williams, R. O'Connor, Archives of Computational Methods in Engineering **6**(4), 279 (1999). DOI 10.1007/BF02818917. URL http://dx.doi.org/10.1007/BF02818917
21. A. Munjiza, K.R.F. Andrews, International Journal for Numerical Methods in Engineering **43**(1), 131 (1998). DOI 10.1002/(SICI)1097-0207(19980915)43:1⟨131::AID-NME447⟩3.0.CO;2-S. URL http://dx.doi.org/10.1002/(SICI)1097-0207(19980915)43:1<131::AID-NME447>3.0.CO;2-S
22. K. Han, D. Peric, D.R.J. Owen, J. Yu, Engineering Computations **17**(6), 680 (2000)
23. S.M. Johnson, J.R. Williams, B.K. Cook, International Journal for Numerical Methods in Engineering **74**(8), 1303 (2008). DOI 10.1002/nme.2210. URL http://dx.doi.org/10.1002/nme.2210
24. R. Verberg, A.J.C. Ladd, Physical Review Letters **84**(10), 2148 (2000). URL http://link.aps.org/abstract/PRL/v84/p2148
25. B. Chun, A.J.C. Ladd, Physical Review E **75**(6), 066705 (2007). URL http://link.aps.org/abstract/PRE/v75/e066705
26. C.K. Aidun, Y. Lu, E.J. Ding, J. Fluid Mech. **373**(-1), 287 (2000)
27. D.R. Noble, J.R. Torczynski, Int. J. Mod. Phys. C **9**(8), 1189 (1998)
28. C.R. Leonardi, B.D. Jones, D.W. Holmes, J.R. Williams, in *DEM 6: Proceedings of the 6th International Conference on Discrete Element Methods and Related Techniques*, ed. by G. Mustoe (2013), pp. 1–8
29. D.J. Holdych, Lattice boltzmann methods for diffuse and mobile interfaces. Ph.D. thesis, University of Illinois at Urbana-Champaign (2003)
30. C.K. Aidun, J.R. Clausen, Annual Review of Fluid Mechanics **42**(1), 439 (2010). DOI 10.1146/annurev-fluid-121108-145519
31. E.J. Ding, C.K. Aidun, Journal of Statistical Physics **112**(3-4), 685 (2003)
32. N.Q. Nguyen, A.J.C. Ladd, Phys. Rev. E **66**, 046708 (2002)
33. L.J. Hou, Z.L. Miskovic, A. Piel, P.K. Shukla, Physics of Plasmas **16**(5), 053705 (2009). DOI http://dx.doi.org/10.1063/1.3138746. URL http://scitation.aip.org/content/aip/journal/pop/16/5/10.1063/1.3138746
34. V.d. Jesus, A. Guimaraes, I. Oliveira, Brazilian Journal of Physics **29**, 541 (1999)
35. Y. Litvinenko, Solar Physics **216**(1-2), 189 (2003). DOI 10.1023/A:1026143310271
36. K. Han, Y.T. Feng, D.R.J. Owen, International Journal for Numerical Methods in Engineering **84**(11), 1273 (2010). DOI 10.1002/nme.2940. URL http://dx.doi.org/10.1002/nme.2940
37. Y. Pappas, D. Klingenberg, Rheologica Acta **45**(5), 621 (2006). DOI 10.1007/s00397-005-0016-8. URL http://dx.doi.org/10.1007/s00397-005-0016-8
38. S. Yiacoumi, D.A. Rountree, C. Tsouris, Journal of Colloid and Interface Science **184**(2), 477 (1996). DOI http://dx.doi.org/10.1006/jcis.1996.0643. URL http://www.sciencedirect.com/science/article/pii/S0021979796906438
39. J. Lindner, K. Menzel, H. Nirschl, Computers & Chemical Engineering **54**(0), 111 (2013). DOI http://dx.doi.org/10.1016/j.compchemeng.2013.03.012. URL http://www.sciencedirect.com/science/article/pii/S009813541300077X
40. W. Hayt, J. Buck, *Engineering Electromagnetics*, 7th edn. (McGraw-Hill, 2006)
41. R. Wolfson, *Essential University Physics*, vol. 2 (Pearson Addison Wesley, 2007)
42. R. Knight, *Physics for Scientists and Engineers: A Strategic Approach* (Pearson Addison Wesley, 2008)
43. T. Zohdi, Archives of Computational Methods in Engineering **17**(2), 109 (2010). DOI 10.1007/s11831-010-9044-3. URL http://dx.doi.org/10.1007/s11831-010-9044-3
44. T.I. Zohdi, *Electromagnetic Properties of Multiphase Dielectrics: A Primer on Modeling, Theory and Computation*, vol. 64, 1st edn. (Springer-Verlag, 2012). DOI 10.1007/978-3-642-28427-4
45. T.I. Zohdi, *Dynamics of Charged Particulate Systems: Modeling, Theory and Computation*, vol. 64, 1st edn. (Springer-Verlag, 2012). DOI 10.1007/978-3-642-28519-6

46. T.I. Zohdi, Journal of Vibration and Acoustics **135**(3), 031007 (2013). DOI 10.1115/1.4023251. URL http://dx.doi.org/10.1115/1.4023251
47. T. Zohdi, Computational Particle Mechanics **1**(1), 27 (2014). DOI 10.1007/s40571-014-0013-8. URL http://dx.doi.org/10.1007/s40571-014-0013-8
48. D. Mukherjee, T.I. Zohdi, Computer-Aided Design **46**, 211 (2014). DOI http://dx.doi.org/10.1016/j.cad.2013.08.034. URL http://www.sciencedirect.com/science/article/pii/S0010448513001747. 2013 {SIAM} Conference on Geometric and Physical Modeling
49. D. Mukherjee, Z. Zaky, T.I. Zohdi, A. Salama, S. Sun, Socity of Petroleum Engineers p. 169639 (2015)
50. E.J. Moniz, H.D. Jacoby, A.J.M. Meggs, The future of natural gas an interdisciplinary mit study. Tech. rep., Massachusetts Institute of Technology Energy Initiative (2011)
51. A.P. Bunger, J. McLennan, R. Jeffrey (eds.), *Effective and sustainable hydraulic fracturing* (InTech, 2013). DOI 10.5772/45724. URL http://www.intechopen.com/books/editor/effective-and-sustainable-hydraulic-fracturing
52. F. Song, H. Kuleli, M. Toksoz, E. Ay, H. Zhang, GEOPHYSICS **75**(6), A47 (2010). DOI 10.1190/1.3484716. URL http://dx.doi.org/10.1190/1.3484716
53. J.E. Drew, H.D. Leslie, P.N. Armstrong, G. Michard. Automated microseismic event detection and location by continuous spatial mapping
54. G. Sleefe, N. Warpinski, B. Engler, *The use of broadband microseisms for hydraulic fracture mapping* (1993). URL http://www.osti.gov/scitech/servlets/purl/10180566
55. D.S. Kim, J.S. Lee, Soil Dynamics and Earthquake Engineering **19**(2), 115 (2000). DOI http://dx.doi.org/10.1016/S0267-7261(00)00002-6. URL http://www.sciencedirect.com/science/article/pii/S0267726100000026
56. H. Sone, M. Zoback, Geophysics **78**(5) (2013)